

Structure of Strained Low-Dimensional Sb by In Situ Surface X-Ray Diffraction

Philip J. Mousley, Christopher W. Burrows, Chris Nicklin, and Gavin R. Bell*

Antimony ultrathin films in tensile strain are grown on InAs(111)B substrates and studied in situ using surface X-ray diffraction. The detailed atomic structures of two highly crystalline Sb(0001) films are derived, with thicknesses of 19 and 4 bilayers. Features considered in structural modeling include interfacial intermixing, surface roughness, individual layer relaxations, and rotational twin domains (RTDs). The four-bilayer film shows significant structural relaxation in every layer, while both films include RTDs. The results are discussed in relation to the topological properties of low-dimensional Sb.

1. Introduction

There is currently great interest in both 2D materials,^[1,2] and materials, 2D or otherwise, which support topologically nontrivial surfaces and interface states.^[3,4] 2D semiconductors offer enormous potential in developing novel heterostructures by layer stacking. Antimony, Sb, is an elemental material which can exist as a 2D layer, dubbed antimonene.^[5–8] In ultrathin-film form (a few atomic bilayers), Sb can also host nontrivial topological order,^[9] exhibiting topological surface and interface states. The remarkable properties of these states, such as spin-momentum locking and suppressed backscattering, offer intriguing possibilities for improved device functionalities, and for Sb and Bi, these are increasingly well understood.^[10] Recent theoretical and experimental studies have examined topological surface states (TSS) on Sb(111).^[11–14] Zhang et al.^[15] presented first-principles calculations demonstrating that increasing the Sb(111) film thickness from 1 to 8 nm causes multiple transitions in the electronic properties of the film. It was shown that as the Sb(111) film thickness increased, the system

transitioned from being in a trivial semiconducting state to a 2D quantum spin Hall state, followed by a 3D topological insulator state, and ending as a topological semimetal. For ultrathin layers the interaction between the upper and lower surfaces becomes increasingly important. This interaction was investigated by Yao et al.,^[16] using scanning tunneling microscopy (STM), who found that altering the film thickness allowed control over the relative contributions from intra- and inter-surface couplings of TSS, highlighting

the potential for tailored transport properties through control of Sb film thickness. Nouri et al.^[17] investigated theoretically the topological phases of 2D Sb (and Bi) and suggested that in the topological crystalline insulator phase, quantized conductance should be robust against disorder.

Antimonene and ultrathin Sb films depend on a suitable substrate for epitaxial growth. Bulk Sb crystals adopt a rhombohedral structure with space group D_{3d}^5 ($R\bar{3}m$), as shown in **Figure 1**. An in-plane symmetry match is achieved between hexagonal Sb(0001) layers and the (111) surfaces of a crystal with cubic symmetry. In this article crystallographic notation refers to the 3-index (*hkl*) format of the cubic unit cell and we hence subsequently refer to Sb(111).

Technologically mature material systems can be advantageous as platforms for new functional materials. Two of the most commonly used semiconductor types are silicon and III–V compounds such as GaAs. Sb has been grown epitaxially on Si surfaces including Si(113),^[18] Si(001),^[19] and various preparations of Si(111).^[9,13,14,20] However, the crystal structure of the Sb overlayer is mismatched with that of the Si substrate in the lattice parameter and/or, symmetry which can lead to island growth, formation of multiple crystallographic domains, etc. Bian et al. used the Bi-terminated Si(111)- $\sqrt{2} \times \sqrt{2}$ R30° as a template for the growth of smooth ultrathin Sb(111) films, which showed spin-polarized surface states coupled to unpolarized quantum well states^[13] and a robust Dirac cone stabilized by strong interaction (chemical bonding) between the film and the substrate.^[14]

A range of in-plane lattice parameters is available among the III–V materials, enabling Sb(111) to be grown with controlled epitaxial stress. The so-called 6.1 Å family offers close in-plane lattice match with interatomic distances across the interface differing by 0.06% (GaSb), –0.6% (InAs), and 0.65% (AlSb) at room temperature. Golding et al. grew Sb epitaxially on both (111)A and (111)B surfaces of GaSb.^[21] They found that careful control over substrate temperature and initial growth rate was

P. J. Mousley, C. W. Burrows, C. Nicklin
Diamond Light Source
Harwell Science Innovation Campus, Didcot, Oxfordshire OX11 0DE, UK

G. R. Bell
Department of Physics
University of Warwick
Coventry CV4 7AL, UK
E-mail: gavin.bell@warwick.ac.uk

 The ORCID identification number(s) for the author(s) of this article can be found under <https://doi.org/10.1002/pssb.202100432>.

© 2022 The Authors. physica status solidi (b) basic solid state physics published by Wiley-VCH GmbH. This is an open access article under the terms of the Creative Commons Attribution License, which permits use, distribution and reproduction in any medium, provided the original work is properly cited.

DOI: 10.1002/pssb.202100432

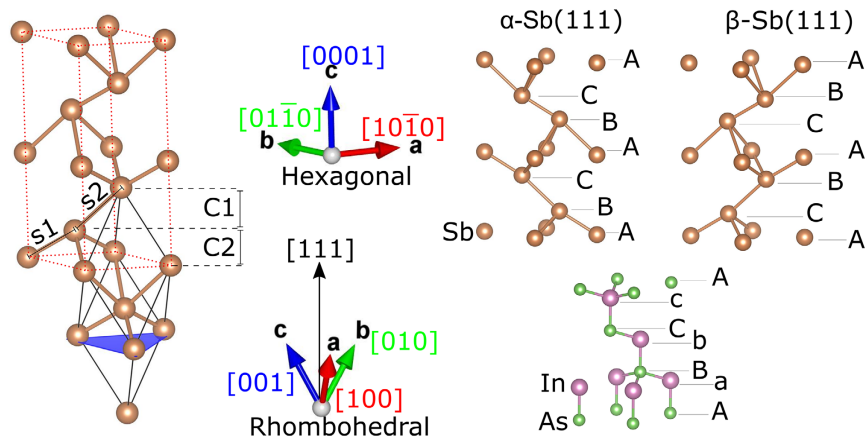


Figure 1. Ball and stick models showing (left) rhombohedral and hexagonal Sb unit cells and (right) layer stacking sequences for untwinned (α -) and twinned (β -) Sb(111) on InAs(111)B. Structural parameters c_1, c_2, s_1, s_2 are listed in Table 2.

essential to maintain single-domain, layer-by-layer epitaxy, and it was possible to grow GaSb(111) on top of Sb thin films to form heterostructures. Guyaux et al. grew GaSb(111) on bulk Sb(111) by interdiffusion (with Ga supply only) and could achieve single-phase epitaxial growth though probably without sharp interfaces,^[22] while Toyota et al. used Sb as a template to improve GaSb growth on Si(111).^[23] Zhou and Wang used density functional theory (DFT) to study a GaSb–Sb superlattice oriented in the [111] direction.^[24] Typical DFT calculations of Sb films have used isolated slabs.^[11,14,15,25]

We are not aware of Sb growth studies on either AlSb or InAs (111) surfaces, though (001) heterointerface formation has been investigated,^[26–28] motivated by interfacial strain and chemical intermixing in conventional III–V superlattice structures, and Sb epitaxy on GaAs(001) has been demonstrated.^[29] InAs(111) surfaces are straightforward to prepare and allow direct growth without a buffer layer. InAs is also interesting in terms of its native electron accumulation layer, which is found at polar surfaces and may depend on surface termination and ordering.^[30–32] Furthermore, we are not aware of any quantitative structural

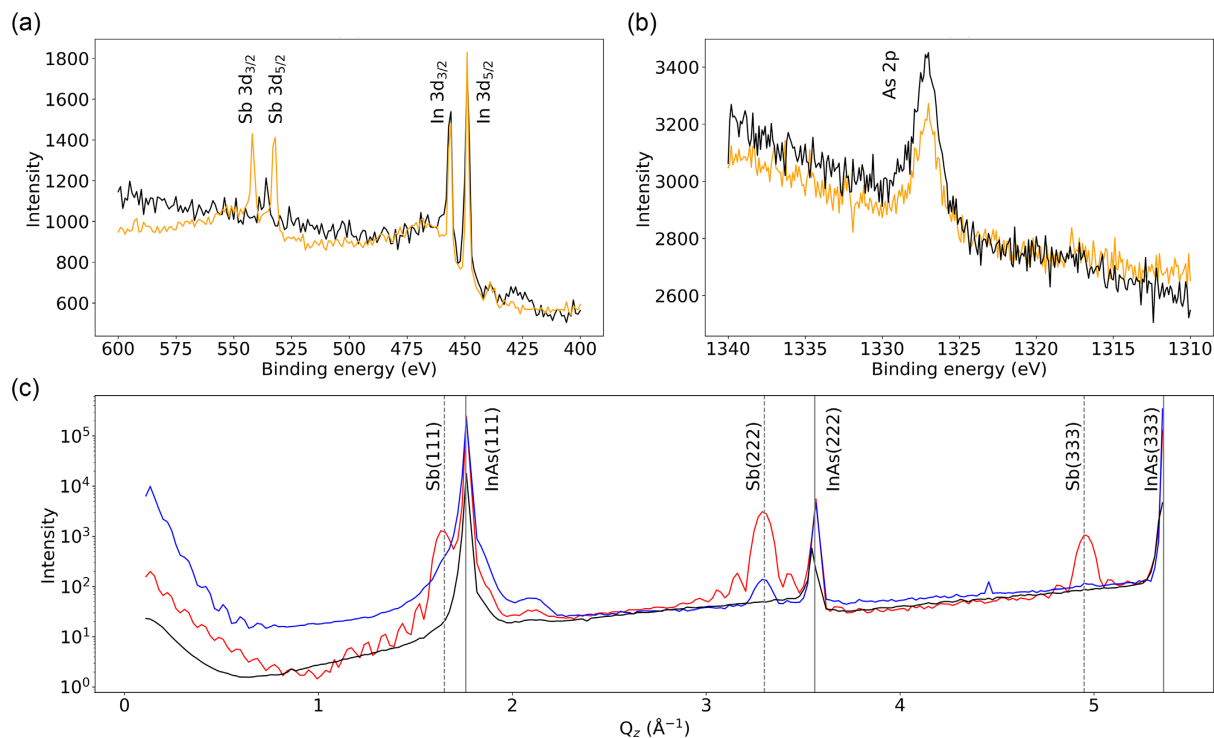


Figure 2. XPS data from clean InAs(111)B (black) and sample 1a (orange) around the a) Sb 3d region and b) As 2p region. c) Specular out-of-plane symmetric X-ray diffraction (XRD) data from sample 1a (black points), 1b (blue points), and 1c (red points). Solid vertical lines show the position of InAs substrate peaks, and dashed vertical lines show positions of Sb film peaks.

studies on Sb ultrathin films. Because interfacial bonding,^[14,25] strain,^[25,33] film thickness,^[15] and extended defects can all influence the electronic structure, it is important to understand the epitaxial relationship, atomic positions around interfaces, surface relaxation and reconstructions, and other crystallographic effects such as dislocations, twinning, and interface geometry.

2. Results

2.1. Sb Film Growth

The clean InAs(111)B surfaces produced sharp (1×1) low energy electron diffraction (LEED) patterns with no sign of fractional-order features. This As-terminated (1×1) surface is

Table 1. Sample preparation summary. T_{cell} is the temperature of the Sb effusion cell, and T_{sub} is the temperature of the InAs(111)B substrate. SXRD datasets were collected immediately after the stages: either or both of CTRs and symmetric out-of-plane diffraction (marked S). * indicates that 1, 6, and 30 min depositions were also performed (data not shown but discussed in the text).

Sample	Process	Time [min]	T_{cell} [°C]	T_{sub} [°C]	Data	Model
a	Sb deposition	20*	430	260	CTR S	Figure 6
b	Sb deposition	20	430	25	S	–
c	Anneal	20	–	210	CTR S	Figure 8
a	Sb deposition	5	430	25	–	–
b	Anneal	20	–	205	CTR S	Figure 10

expected for preparation by sputtering and annealing.^[34–36] No fractional-order spots were observed after any Sb deposition. Typical X-ray photoelectron spectroscopy (XPS) data for clean InAs(111)B substrate and sample 1a are shown in **Figure 2**. Panels (a) and (b) show the In 3*d* and As 2*p* peaks, respectively, from the substrate (black lines) and sample 1a (orange lines). No features due to oxygen or carbon are present. For sample 1a (**Table 1**), the Sb 3*d* peaks appear and As 2*p* is attenuated but still clearly detectable. There is almost no change in the In 3*d* peaks. One would expect Sb layer to attenuate the In and As signals due to the inelastic scattering of photoelectrons passing through it. The inelastic mean free path of electrons in Sb can be estimated as 0.67 nm at kinetic energy 158 eV (corresponding to the As 2*p* level) and 2.3 nm at 1031 eV (In 3*d* level).^[37] A single bilayer of Sb on top of InAs would be expected to attenuate the As 2*p* signal by around 50% and the In 3*d* signal by less than 10%. The observed reductions are smaller than these, suggesting that Sb forms an even thinner or an incomplete layer or is intermixed with the surface atoms of InAs. As shown later, an interpretation of partial surface As replacement by Sb is supported by the surface X-ray diffraction (SXRD) data for this high-temperature Sb exposure.

Specular XRD data are shown in **Figure 2c**. Following the increased temperature in Sb deposition, sample 1a (black line) shows no epitaxial Sb signal, which would be expected for As–Sb intermixing only in the surface layers. In contrast, room-temperature Sb deposition used for sample 1b (blue line) shows weak peaks due to epitaxial Sb(111). After annealing to obtain sample 1c (red line), these Sb peaks become much more

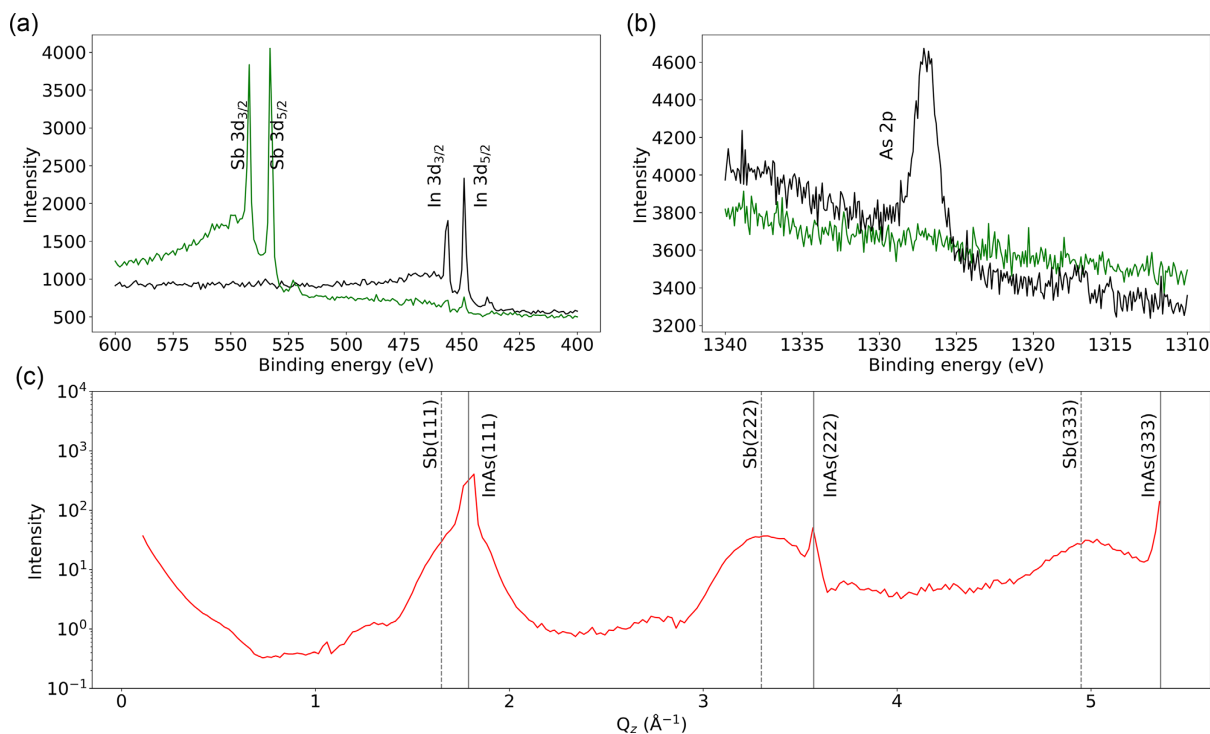


Figure 3. XPS data from clean InAs(111)B (black) and sample 2b (green) around the a) Sb 3*d* region and b) As 2*p* region. c) Specular out-of-plane symmetric XRD data from sample 2b. Solid vertical lines show the position of InAs substrate peaks, and dashed vertical lines show positions of Sb film peaks.

intense and clear Laue oscillations appear. Fitting these gives a film thickness of 7.04 ± 0.18 nm. It therefore appears that low substrate temperature (25°C) favors Sb sticking and film growth, while annealing to 210°C is sufficient to produce good crystalline order and uniformity in the Sb films.

Similar data for sample 2b are shown in **Figure 3**. After shorter deposition with the sample held at room temperature, followed by annealing, the In $3d$ and As $2p$ XPS peaks are almost completely attenuated, while the Sb $3d$ peaks are intense (green lines). This indicates full coverage by Sb film of at least around 1 nm thickness, taking into account the inelastic mean free paths and the take-off angle of the XPS analyzer. In specular XRD, broad Sb(111) peaks appear, suggesting a very thin but epitaxial Sb film. No evidence in SXR D was seen for plastic relaxation, that is, both films appeared fully coherently strained to the substrate in-plane lattice parameter.

Figure 4 shows four atomic force microscopy (AFM) images of Sb–InAs(111)B samples. Panel (a) shows a 60-bilayer Sb film grown under slightly different conditions in a separate epitaxy chamber. The Sb film has formed a distinctive morphology of

triangular island-like structures. Bilayer-height facets are distinguishable on the sides of many islands and the island sides range from 0.4 to $1.5\ \mu\text{m}$ in length. The island height is up to 6 nm peak to trough, which is much smaller than the average film thickness of 23.5 nm. The film covers the substrate surface fully but has developed a nonplanar surface morphology related to its hexagonal crystal structure. In contrast, the thinner films studied by SXR D present a far more conformal, flat surface morphology. An AFM image of a 19-bilayer-thick in situ-grown sample is shown in (b). Typical terraces are more than 100 nm wide, with height fluctuations of the surface around 1 nm. Some stripy patterns can be discerned within terraces (running diagonally from top left to bottom right in this image). These likely reflect the underlying step-terrace structure of the slightly miscut InAs(111) surface. This phenomenon is more clearly seen in images (c) and (d) of a four-bilayer-thick sample, where a mean terrace width of around 110 nm is observed. This corresponds to a local miscut of 0.18° . A height profile is shown in the inset in panel (c), which highlights the step-terrace structure. These observations show that the thin Sb films are conformal to the

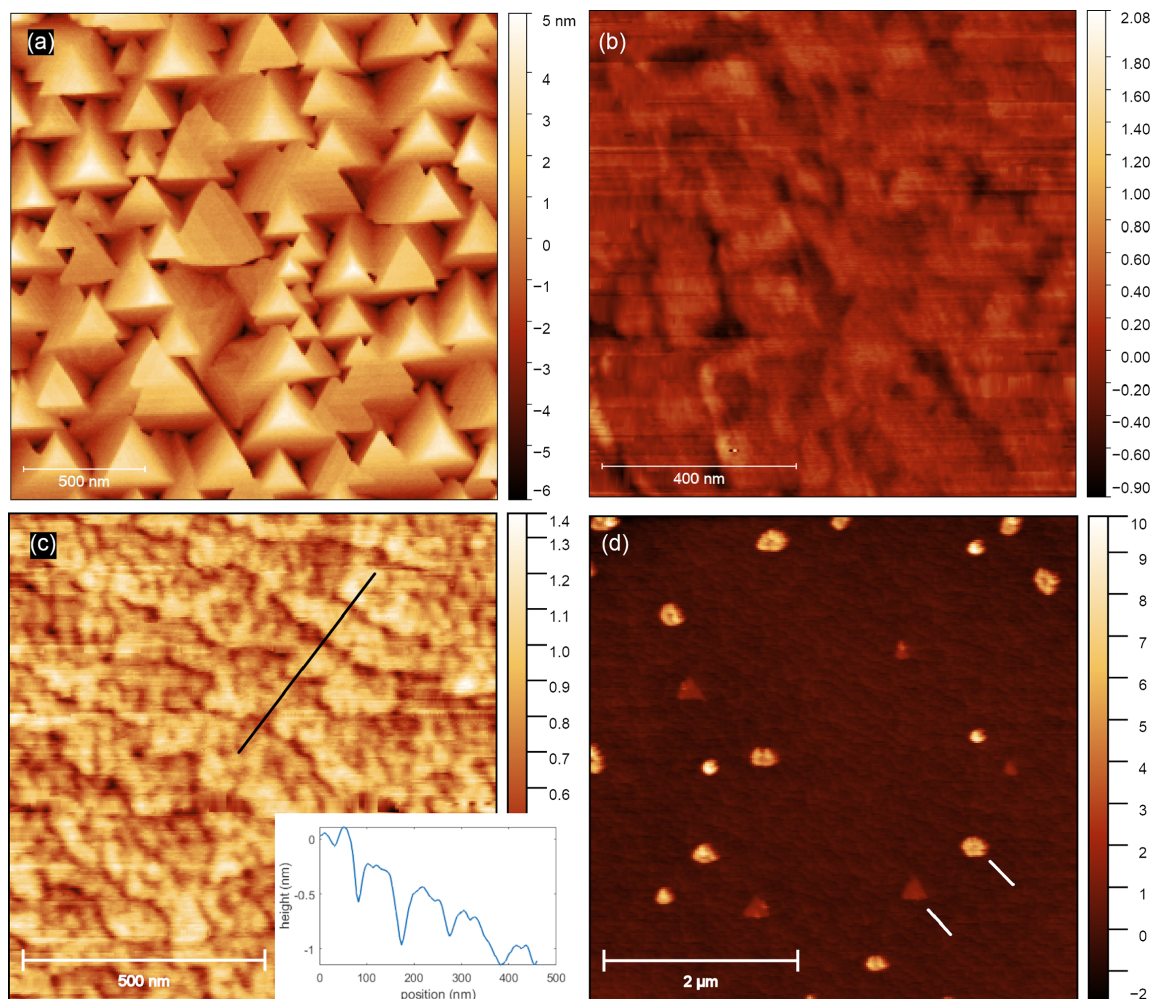


Figure 4. AFM topographs of three Sb–InAs(111)B surfaces. a) 60-bilayer film, grown separately, at $2\ \mu\text{m}$ image size; b) 19-bilayer Sb film (sample 1c) at $1\ \mu\text{m}$ image size; c) 4-bilayer Sb film (sample 2b) at $1\ \mu\text{m}$ image size; and d) 4-bilayer Sb film (sample 2b) at $5\ \mu\text{m}$ image size. In (c), a height profile is shown (black line and inset) and in (d), a triangular and a globular feature are each highlighted with white dashes.

substrate; the underlying step-terrace structure is shown quite clearly for the ultrathin film and is somewhat obscured by the thicker film. Some larger triangular and globular features can also be seen in (d), with examples highlighted by white dashes. The triangular features are flat and consistently aligned: they are likely to be Sb islands on top of the conformal 2D Sb layer (they may subsequently nucleate the more 3D islands found in thicker films). The globular features are surface contamination from sample handling ex situ. Additional height profiles are given in Supporting Information.

2.2. Sample 1a

After data reduction, the crystal truncation rod (CTR) dataset comprised nine symmetrically independent CTRs (386 data points). The CTR profiles (Figure 5) were fitted using InAs(111)B-(1×1) bulk model with Sb substitution on As sites. The free parameters were individual [111] displacement parameters for the top six atomic layers, fraction of Sb substitution at surface As atomic sites, an overall layer occupancy parameter for the top two atomic layers, and a global scaling factor. The best fit ($\chi^2 = 2.172$) was obtained with a 55% occupancy of the top bilayer, in which $7.5\% \pm 2.5\%$ of As atoms is substituted for Sb. The fitted structure is summarized in Figure 6. The most significant subsurface structural changes

are expansions of the In–As atomic bilayers by $4\% \pm 2\%$ (layers 5–6) and $9\% \pm 3\%$ (layers 3–4) over the bulk value of 0.8741 Å. The outermost partially occupied In/As–Sb bilayer is expanded by $20\% \pm 4\%$ over the bulk spacing due to outward relaxation of the As–Sb layer. There is no evidence for the formation of any antimonene-like structure, that is, a complete Sb layer terminating the crystal. Note that fitting of the InAs(111)B clean surface CTR data (not shown) was achieved with a fully occupied top bilayer, so the Sb flux exposure at 260 °C induced step-terrace structures or 2D islands at the surface comprising roughly half a layer of InAs_{0.95}Sb_{0.05}.

The effect of duration of Sb flux exposure for increased substrate temperature ($T_{\text{sub}} = 220$ °C) was investigated on a different sample by interrupting growth at various times (1, 6, and 30 min) and obtaining CTR data. For all deposition times on this sample, the CTR data collected were identical (Figure S1, Supporting Information), and XPS data also showed similar Sb 3*d* intensities after both 6 and 30 min of deposition. The similarities of CTR and XPS data after various deposition times suggest that the Sb–As substitution occurs quite rapidly at high temperatures, finding an equilibrium structure within a few minutes at the flux used. Subsequent Sb exposure does not increase the Sb film thickness or substituted fraction, that is, the sticking coefficient on the Sb-substituted surface is zero for $T_{\text{sub}} = 220$ –260 °C.

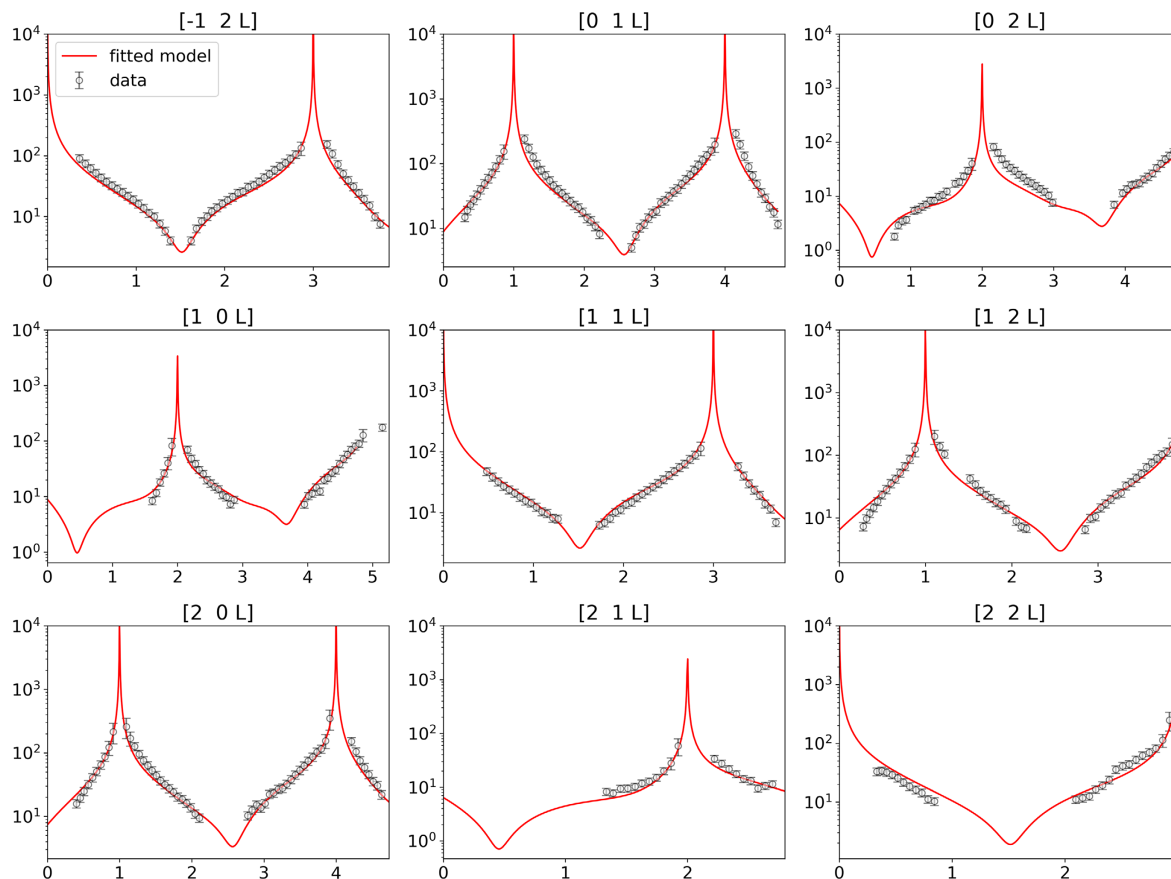


Figure 5. CTR data for sample 1a. The axes are structure factors (vertical) and *L* index (horizontal) for each $[HKL]$ rod. Red lines show the best fits from the surface substitution model.

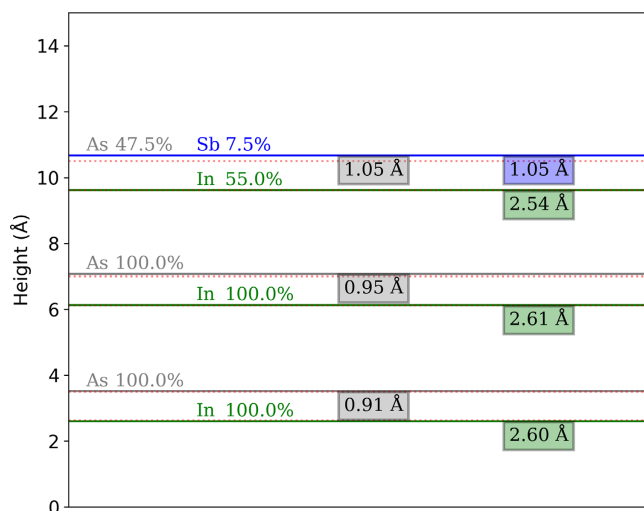


Figure 6. Schematic layer diagram for best fit model to sample 1a. Solid gray lines show the heights of the As layers, solid green lines show heights of the In layers, and the dotted red lines show the expected positions of InAs layers if the bulk spacings (0.87 and 2.62 Å) are continued. The distance value below each line is the separation between that layer and the layer below.

2.3. Sample 1c

CTR data were obtained after postdeposition anneal. After data reduction, the CTR dataset comprised seven symmetrically independent CTRs (899 data points) and is shown in **Figure 7**. Following the specular XRD (Figure 2c), the CTR data were fitted using a model of Sb(111) bilayers on top of InAs(111)B-(1×1) surface. The number of Sb bilayers was varied in a small range around that corresponding to the film thickness used to fit the Laue oscillations (Figure 2). Individual [111] displacement parameters were used for the top six InAs atomic layers, as well as the four atomic Sb layers closest to either the Sb/InAs interface or sample surface. To reduce the number of total fitting parameters, the central stack of 29 Sb atomic layers located away from either the interface or the surface had a common pair of [111] displacements (which were optimized as part of the fitting). We also allowed variation in both the Sb surface atomic layer occupancies and the fraction of Sb substituted at the interface As sites. Because the substrate surface formed by the first deposition has incomplete final layer occupancy, the Sb occupancy parameter was included for each of the top three InAs atomic layers. We also accounted for the possibility of rotational twin domains (RTDs) in the model. The twin structures are

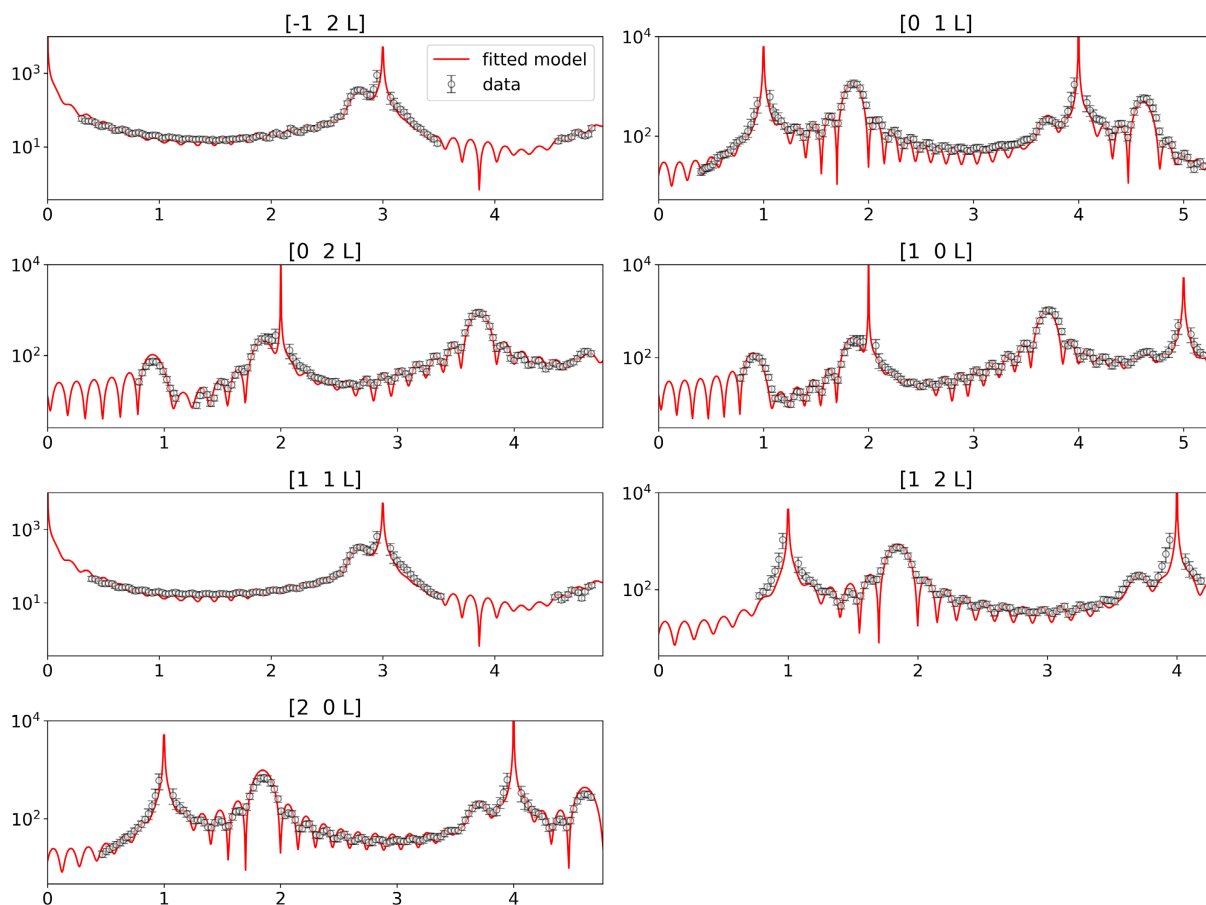


Figure 7. CTR data for sample 1c. The axes are structure factor (vertical) and L index (horizontal) for each $[HK]$ rod. Red lines show the best fit model.

summarized in Figure 1. Following convention for RTD formation on (111) surfaces,^[38,39] the twinned and untwinned domains are referred to as α -Sb(111) and β -Sb(111), respectively. The registry between α -Sb(111) and the InAs substrate was Sb atoms on face-centred cubic (FCC)-like adsorption sites and β -Sb(111) on hexagonal close-packed (HCP)-like sites. Note that extensive modeling work has been performed with different combinations of physically plausible structural parameters, and all of the earlier features are required to optimize fits. In addition to RTDs, stacking faults were included in the Sb layer models, but these did not prove favorable in optimizing fits and were therefore rejected. Interfacial intermixing and surface roughness are represented in our models by the layer occupancy parameters rather than a beta roughness model. For both samples, the strong Laue oscillations and/or oscillatory CTR behavior confirm that the films have sharp interfaces and flat surfaces.

The best fit model to the CTR data ($\chi^2 = 2.711$) is summarized in **Figure 8** and has a total Sb thickness of 7.23 ± 0.12 nm (38 Sb layers) with $95\% \pm 1\%$ α -Sb(111) and $5\% \pm 1\%$ β -Sb(111) domains. The Sb surface occupancy declines over the top four layers ($84\% \pm 2\%$ in layers 3–4 and $11\% \pm 2\%$ in layers 2–1), reflecting the low surface coverage by flat-topped islands sitting on top of the main conformal film (Figure 4d). At the InAs–Sb interface, there is only strong elemental mixing in the top two bilayers. The terminating InAs-like bilayer contains $84\% \pm 6\%$ Sb substitution in its group-V monolayer, while the In monolayer only contains 55% In, the other atomic sites being filled with Sb. This is consistent with the sample history, with an overall atomic occupancy of 55% in the terminating bilayer after the first Sb deposition. The InAs bilayer below this interface has $32\% \pm 4\%$ Sb replacing As. This suggests that intermixing due to bulk atomic exchange is minimal, as expected at the low temperatures used, and that the nonideality of the interface is predominantly due to the substrate surface morphology (atomic-height terraces and islands).

The first full Sb bilayer above the interface is compressed of $5\% \pm 2\%$ compared with bulk spacing, dropping to $3\% \pm 2\%$ compression in the second full Sb bilayer. Bulk values for the Sb layer spacings are then recovered. Significant structural distortions only occur in InAs in the two mixed bilayers. The penultimate bilayer (with 32% Sb replacing As) is expanded by $13\% \pm 3\%$, while the terminating bilayer (with both In–Sb and Sb–As mixing) has a spacing of 1.28 \AA , close to the average of the InAs bilayer and Sb bilayer spacings (1.20 \AA).

2.4. Sample 2b

The dataset consisted of nine symmetrically independent CTRs (928 data points, **Figure 9**). Due to wider oscillations and a very strong CTR signal, structure factor errors for this dataset were reduced to 10% for data points not close to Bragg values in L . Fitting the data from sample 2 used a model with 14 atomic layers (3 InAs bilayers and 8 layers of Sb) allowed to move in the [111] direction. The occupancy of the upper three Sb layers could vary, and the model included RTDs as well as Sb substitution in the interfacial As layer. The best fit model to the CTR data ($\chi^2 = 2.6806$) comprised $7\% \pm 1\%$ β -Sb(111) and $92\% \pm 1\%$ α -Sb(111), with $35\% \pm 2\%$ Sb substitution at the interface As

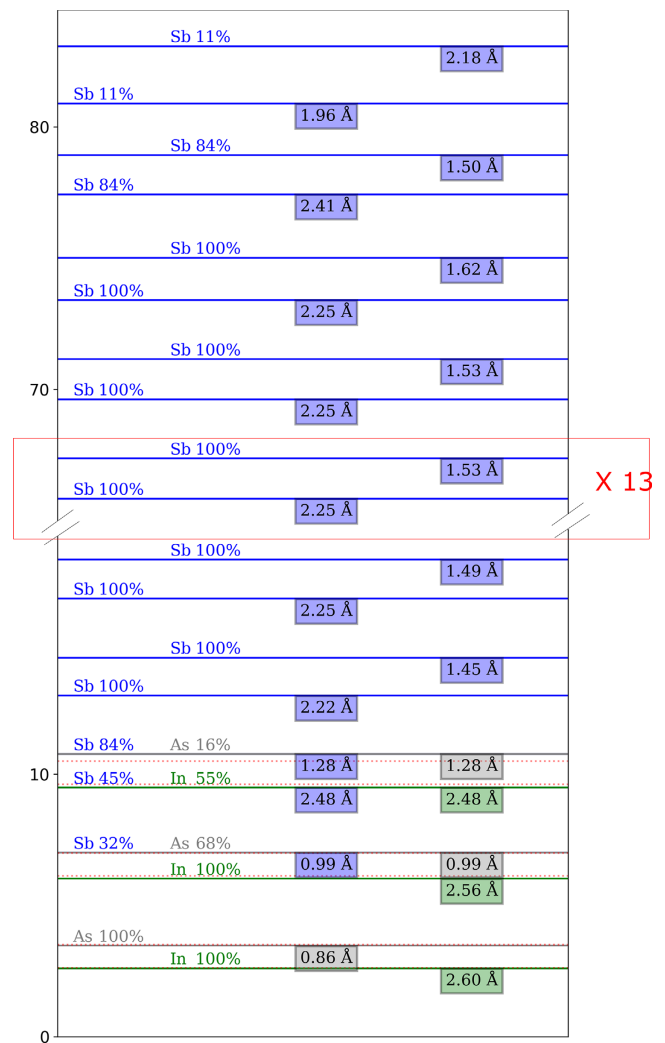


Figure 8. Schematic layer diagram for best fit model to sample 1c. Solid gray lines show the heights of the As layers, solid green lines show heights of the In layers, and the dotted red lines show the expected positions of InAs layers if the bulk spacings (0.87 and 2.62 \AA) are continued. The bulk spacings of unstrained Sb would be 1.506 and 2.251 \AA . The distance value below each line is the separation between that layer and the layer below.

sites. The occupancy of the surface layers is much higher than that for the thicker film, with layers 2 and 3 $88\% \pm 1\%$ occupied and the surface layer $63\% \pm 1\%$ occupied. A summary of the model is given in **Figure 10**.

3. Discussion

Sb deposition with the substrate at $260 \text{ }^\circ\text{C}$ causes self-limiting Sb–As exchange with incorporation of 7.5% Sb on As sites in the topmost atomic layer only. Several groups have investigated Sb/As intermixing in the context of InAs/GaSb heterostructure growth by molecular beam epitaxy. For example, using in situ XPS, Wang et al. showed that Sb exchange at the surface As sites occurs on exposure of InAs(001) at $380 \text{ }^\circ\text{C}$ to a flux of Sb_2 ^[40].

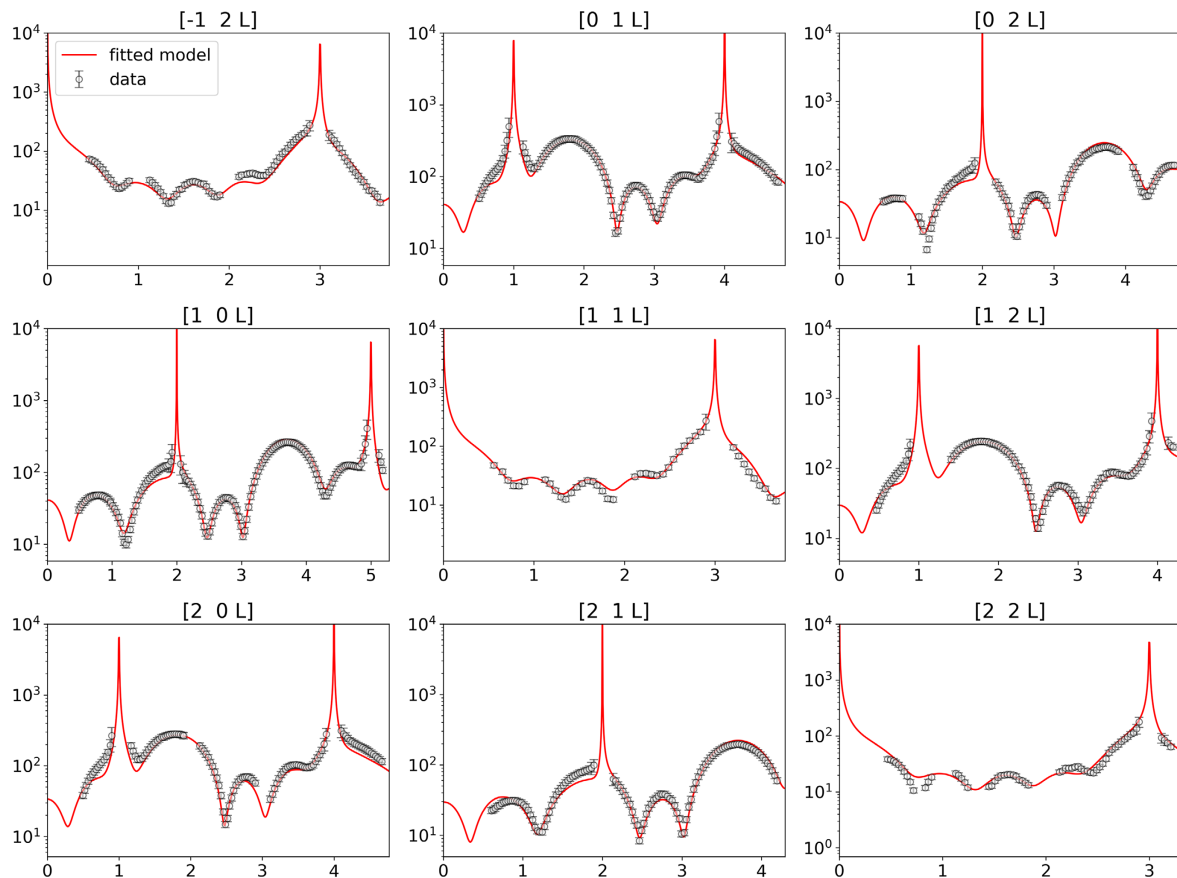


Figure 9. CTR data for sample 2b. The axes are structure factor (vertical) and L index (horizontal) for each $[HK]$ rod. Red lines show the best fit model.

Although they were not able to quantify layer compositions based on XPS alone, they found a strong reduction in Sb–As exchange for Sb_4 versus Sb_2 flux. The source in the present experiment produces only Sb_4 . Anderson and Millunchick^[28] studied the interaction of Sb_2 and As_2 with $\text{InAs}(001)$ at 425°C and found a rich phase diagram of surface reconstructions both experimentally and using DFT. In nearly all cases, Sb incorporated only in the outermost atomic layer, the exceptions being highly Sb-rich “Sb-dimer-on-anion” reconstructions such as $c(4\times 4)$. The present experiments reach a qualitatively similar equilibrium with Sb incorporation only in the outermost atomic layer. To explain how the sticking coefficient for Sb_4 becomes zero after a small fraction of an atomic layer is incorporated, we hypothesize that the pre-existing surface sites related to defects or steps could be “saturated” with incoming Sb, with subsequent Sb unable to stick. It could also be the case that a fraction of a monolayer of metallic In is left at the surface, residual from ion sputtering,^[31] which reacts with incoming Sb (Sb reacts readily with In during heteroepitaxy^[41,42]). A combination of these effects could give rise to the observed dependence on total Sb exposure and the reduced occupancy of the mixed layer. Anderson and Millunchick observed atomic bilayer-height islands appearing when In was predeposited on $\text{InAs}(001)$ before Sb_2 exposure to control the final surface reconstruction.^[28] This suggests that a supply of surface In may well promote 2D island growth during Sb exposure, as seen for sample 1 here.

The Sb epilayer growth results can be summarized as follows. 1) Room-temperature deposition of Sb on to $\text{InAs}(111)\text{B}$ allows the growth of thin films, which become epitaxial and highly crystalline on annealing to around 210°C . 2) Intermixing of elements at the Sb/ InAs interface depends on sample history with a lowest value of 35% Sb incorporation into the substrate’s outermost As layer only. 3) Twinning occurs in the Sb films with up to 7% RTD present dependent on sample history. 4) Significant structural relaxation is confined to the surface and interface bilayers and adjacent layers (relaxation occurs in all bilayers for the four bilayer-thick films).

Hilner et al.^[35] observed a stacking fault-related effect on clean $\text{InAs}(111)\text{B}$ surfaces after high-temperature oxide desorption under As flux. On cooling, the melted surface recrystallized into wurtzite-stacked as well as regular zincblende 2D islands.^[35] Our best fit models contained no stacking faults in the InAs , and only RTDs in the Sb overlayer, indicating that sputtering with a lower-temperature anneal does not induce such defects. The presence of RTDs in the Sb layer is consistent with the previously reported Sb growth on GaSb ,^[43] where the lattice mismatch is similar. Twinning has been observed in bulk Sb crystals, which in the full rhombohedral structure manifests in a small angular offset between twinned and untwinned (111) planes. On cleaving $\text{Sb}(111)$ crystals, this leads to the formation of twinned terraces 2.45° apart, which have been detected by STM.^[44] In the present case, we modeled the Sb films in the hexagonal (111) structure

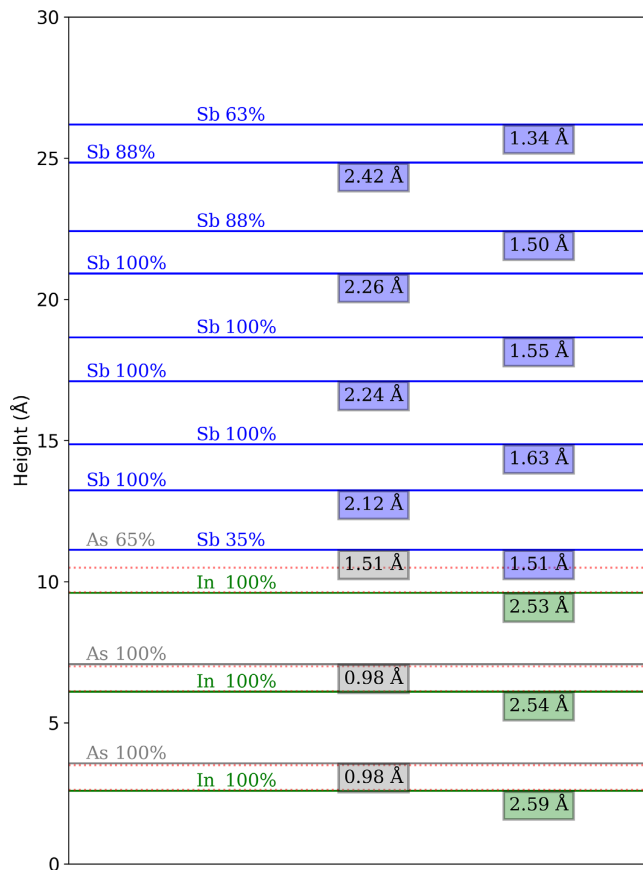


Figure 10. Schematic layer diagram for best fit model to sample 2b, with all layer spacing values given in Å. The dotted red lines show the expected positions of InAs layers if the bulk spacings (0.87 and 2.62 Å) were continued. The bulk spacings of unstrained Sb would be 1.506 and 2.251 Å. The distance value below each line is the separation between that layer and the layer below.

for which twinning does not change the basal plane angle. It is not clear what effects the extended defects at RTD boundaries have on the bulk electronic band structure. Yao et al.^[16] beautifully demonstrated the effect of Sb film thickness (4–30 bilayers) on the coupling of the top surface to bottom surface (interface) TSS for Sb(111) on Bi-terminated Si(111) using quasiparticle interference (QPI) measured in STM. The sixfold symmetric QPI patterns should not be affected by RTDs. However, RTDs would affect any measurement of spin textures or scattering underpinned by threefold surface symmetry; we are not aware of any recent works where RTDs are considered.

Lattice measurements of the best fit structures for both room-temperature depositions, along with previous published experimentally obtained values for bulk Sb, are shown in **Table 2**. Along the [111] direction, c_1 is the intrabilayer spacing (corresponding to covalent bonds) and c_2 is the interbilayer spacing (corresponding to mainly van der Waals interaction). s_1 and s_2 are the smaller intrabilayer and larger interbilayer atomic bonding distances, respectively. The fit SXR structural parameters vary from layer to layer in our films. For sample 1c (19 bilayers), the tabulated values are the common layer separations in the central slab of Sb

Table 2. Structural parameters in Å for best fit SXR models (first two rows), as well as parameters previously reported for bulk crystals. Parameters c_1 and c_2 are Sb layer separations (Figure 1). They vary from bilayer to bilayer in the different structures, as shown in Figure 8 and 10. For sample 1c (19 BL), we quote the repeated central slab values. In contrast, for sample 2b (4 BL), values have been put in parenthesis to highlight the limitations on interpreting these average structural lattice values from a very small number of atomic layers. The study by Stegemann^[44] reports the bilayer cleavage step height at 3.75 ± 0.1 Å (*) consistent with other $c_1 + c_2$ values. DFT calculations report free-standing films and bulk, and the functional use is noted (LDA: local density approximation, GGA + D: generalized gradient approximation with dispersion correction, and bare GGA).

Dataset	a	c	c_1	c_2	s_1	s_2
bilayer (1c)	4.284	11.34 ± 0.03	1.53	2.25	2.91	3.34
bilayer (2b)	4.284	(11.31)	(1.51)	(2.26)	(2.90)	(3.35)
Expt. ^[45]	4.3084	11.274	1.506	2.251	2.908	3.355
Expt. ^[44]	4.31	–	*	*	–	–
Expt. ^[51]	4.30	11.340	1.540	2.240	2.921	3.344
LDA film ^[15]	4.006	–	1.509	2.146	–	–
GGA + D film ^[5]	4.06	–	1.66	–	–	–
GGA + D film ^[6]	3.94	–	1.55	–	2.76	–
GGA + D bulk ^[6]	4.13	–	1.54	–	2.84	–
GGA bulk ^[52]	4.386	11.573	1.508	2.349	2.947	3.454

layers away from the interface and surface layers (Figure 8). However, for sample 2b (four bilayers), there is strong variation throughout the film and we give the mean layer separation values. Relatively large structural relaxations are observed near the surface for the low-occupancy top layers of the 19-bilayer film. This phenomenon may be related to Sb atoms with lower coordination found near the peaks of shallow pyramidal structures on top of the main film. We have previously observed such structures in thicker Sb films by AFM.

For sample 1c, the expansions for the second and third Sb bilayer nearest to the surface are $-2\% \pm 2\%$ and $6\% \pm 2\%$, respectively, with an interbilayer expansion of $7\% \pm 2\%$ between them. Structural distortions are of similar magnitude at the mixed interface layers. Another notable effect is the transition to the pure Sb region from the mixed Sb–As film terminating the substrate, with the $c_1 + c_2$ sum increasing for bilayers further away from the interface until reaching the bulk value in the Sb central slab. Wang and Ding^[5] calculated the electronic structures of heterobilayers of As/Sb with Si/C, finding that the bandgap of Sb/Si sheet was adjustable by perpendicular strain with a deformation potential of 0.2 eV Å⁻¹. While they suggested that high-pressure experiments and intercalation could be used to investigate this modulation of electronic structure experimentally, it is clear from our results that significant “natural” variations in basal plane spacings occur in real epitaxial Sb thin films. In the case of sample 2b, the total Sb bilayer thickness is consistent across the four bilayers, with a mean value of 3.76 Å and standard deviation of 0.02 Å. However, the intra- and interbilayer spacings vary greatly, with the ranges of c_1 and c_2 both being ≈ 0.3 Å. These large relaxations could cause very significant

modulations of the electronic structure. Error bars on the fit structural parameters are discussed in Supporting Information.

Using a bulk Sb lattice parameter of $a = 4.3084 \text{ \AA}$ ^[45] and the measured InAs(111) substrate lattice parameter of $a = 4.2840 \text{ \AA}$, we calculate the Matthews–Blakeslee critical thickness for the formation of edge dislocations in Sb to be $\approx 18 \text{ nm}$. Both Sb films studied here should remain fully strained in-plane, as is observed. The in-plane and out-of-plane strains are -0.57% and $+0.55\%$ respectively, indicating a nonisochoric deformation consistent with the elastically anisotropic film. The possibility to grow highly crystalline Sb films with well defined epitaxial strain is demonstrated. This is important for optimization of 2D heterostructures and topological thin films as biaxial strain has been predicted to have significant effects. In the case of semiconducting arsenene and antimonene, increasing tensile in-plane strain reduces the bandgap at the Brillouin zone center (as calculated with a hybrid functional in DFT), inducing a transition from indirect- to direct-gap behavior.^[6] Despite Sb being in a predicted topologically trivial state below four bilayers,^[15] Chuang et al.^[33] found that as tensile strain increased in a single Sb bilayer, the bandgap narrowed and then inverted, inducing a topologically nontrivial phase. We are not aware of DFT studies on strained multibilayer Sb films, nor of studies focusing on compressive strain. With a large lattice mismatch of 11.9%, Sb films on Bi-terminated Si(111) relax fully even at very low thickness, with ordered misfit dislocation arrays.^[14,16] The present choice of the substrate enables coherent strain over a wide range of Sb film thicknesses and opens up the possibility of strain and band structure engineering in topologically nontrivial films. Virtual substrates can be used to lattice match materials for heteroepitaxy.^[46] In the present case, $\text{InAs}_{1-x}\text{Sb}_x$ could be used to controllably strain Sb ultrathin films between -0.57% ($x = 0$) and $+6.5\%$ ($x = 1$). The tensile strain would be sufficient for induced band inversion in antimonene.^[33]

4. Conclusion

The growth of highly crystalline, coherently strained, and conformal Sb epitaxial films on InAs(111)B has been demonstrated with in-plane compressive strain of -0.57% . For both 4-bilayer and 19-bilayer films, expected to be 2D quantum spin-Hall phases and 3D topological insulators, respectively,^[15] the full atomic structures were derived from in situ SXRDX supported by XPS and AFM. There was some intermixing of atomic species at the interface, minimized by direct growth at room temperature to 35% Sb substitution of As in the outermost InAs layer. Almost all of the 19-bilayer film was in a uniform strain state, $+0.55\%$ out of plane, with 6% expansion in the outermost full bilayer. Each bilayer of the 4-bilayer film showed very similar total width, but the intra- and interbilayer spacings varied strongly throughout the film with a range of 0.3 \AA . The films were twinned, including 5% or 7% RTDs. The RTDs would affect spin texture or scattering measurements underpinned by threefold surface symmetry. The ability to coherently strain these films opens up the possibility for band structure engineering in topologically nontrivial materials within a mature semiconductor material family. Theoretical investigations based on realistic strained structures with a III–V substrate would be valuable.

5. Experimental Section

Sample Preparation and Analysis: All SXRDX measurements were performed at the ultrahigh vacuum (UHV) EH2 end station on the I07 beamline of Diamond Light Source.^[47] The photon energy was 12.5 keV (0.99 \AA) and scattering was recorded using a PILATUS 100 K 2D detector. Sb thin films were deposited in the SXRDX scattering chamber. InAs(111)B substrates were cleaved into $10 \text{ mm} \times 10 \text{ mm}$ samples and then indium bonded to sample plates and loaded into the UHV system. The samples were then cleaned using cycles of Ar-ion bombardment (500 eV) and 30 min anneals at substrate temperature $T_{\text{sub}} = 410 - 440 \text{ }^\circ\text{C}$. Depositions were conducted using a Knudsen effusion cell, and the thin-film growth was analyzed in situ using a combination of CTR scans, out-of-plane symmetric (specular) XRD, LEED, and XPS. The XPS used nonmonochromatized Al K α radiation and a take-off angle of 43.4° ; due to a malfunction, it was not possible to measure XPS from sample 1c. The out-of-plane symmetric XRD scans were taken in sections either side of the strong InAs(111) Bragg peaks to avoid saturation of the detector. AFM was used to characterize the surface morphology of both in situ-grown ultrathin Sb films and thicker films grown separately.

We focus on two Sb thin-film samples in this article. Sample 1 had an initial Sb layer deposited using a high substrate temperature of $T_{\text{sub}} = 260 \text{ }^\circ\text{C}$ (1a), followed by a second Sb deposition stage at room temperature (1b). Sample 2 had a single shorter Sb deposition stage at room temperature (2a). Both samples were annealed postgrowth to just above $T_{\text{sub}} = 200 \text{ }^\circ\text{C}$ (1c and 2b). The thickness of sample 1 was calculated from intensity oscillations present in out-of-plane specular XRD data, as well as the CTR line profile fitting. However the thickness of sample 2 could only be measured using CTR line profile fitting due to a lack of usable interference oscillations in the out-of-plane XRD data.

SXRDX Data Analysis: The samples were all aligned using a hexagonal InAs(111)B- (1×1) unit cell, with lattice parameters $a = b = 4.284 \text{ \AA}$ and $c = 10.493 \text{ \AA}$. Horizontal axes on the CTR plots were the “L index,” that is, L measured in reciprocal lattice units corresponding to this InAs unit cell. CTR data reduction was carried out using a modified version of the package Scanalysis created by Schlepütz et al.^[48] Once CTR intensity profiles were extracted and had appropriate corrections applied (polarization, rod intercept, and active area), the line profile datasets were analyzed using ROD^[49] to enable structure refinement via χ^2 -minimization procedure. Unless stated otherwise, error values for calculated structure factors were set to 15%, with increased error for data points close to integer Bragg values in L . Error analysis is discussed further in the Supporting Information. Crystallographic factors investigated in the fitting included atomic layer occupancy (Sb, In, As, vacancy), twinning, interface geometry, and structural relaxations.

The InAs(111) wafer had a small crystallographic miscut, which necessitated a slightly modified methodology for data extraction. Crystallographic miscut caused the CTR signal appearing on a 2D detector to be split into subrod signals when near the anti-Bragg positions.^[50] For the data analysis reported in this article, if the two subrod signals were close enough together, a single region of interest could be used to surround both signals. However when the subrod signals were further apart, the background fitting algorithm failed. When this was the case, there was always one of the subrod signals which was much stronger in intensity. Using a test section of a CTR with subrod signals present, both subrod signals were measured separately and combined to give a total dataset. It was found that due to its low intensity, the weaker subrod signal had negligible influence on the overall line profile of the CTR. Therefore, a single region of interest was used for all CTRs, and in images which had two subrod signals separated far apart, the signal region of interest was centered on the dominant subrod signal. All regions of interest located slightly away from the center of the detector had appropriate corrections to L values applied.

Supporting Information

Supporting Information is available from the Wiley Online Library or from the author.

Acknowledgements

This work was carried out at Diamond Light Source during experiment S113769. The authors are grateful to M. Forster and J. Rawle for support and to I. Elhousieny and T. Rehaag for assistance with offline molecular beam epitaxy and atomic force microscopy.

Conflict of Interest

The authors declare no conflict of interest.

Data Availability Statement

The data that support the findings of this study are available from the corresponding author upon reasonable request.

Keywords

antimony, crystallography, strains, surface X-ray diffraction, topological materials

Received: August 25, 2021

Revised: December 14, 2021

Published online:

- [1] S. Z. Butler, S. M. Hollen, L. Cao, Y. Cui, J. A. Gupta, H. R. Gutierrez, T. F. Heinz, S. S. Hong, J. Huang, A. F. Ismach, E. Johnston-Halperin, M. Kuno, V. V. Plashnitsa, R. D. Robinson, R. S. Ruoff, S. Salahuddin, J. Shan, L. Shi, M. G. Spencer, M. Terrones, W. Windl, J. E. Goldberger, *ACS Nano* **2013**, *7*, 2898.
- [2] M. G. Stanford, P. D. Rack, D. Jariwala, *npj 2D Mater. Appl.* **2018**, *2*, 20.
- [3] C. Kane, J. Moore, *Phys. World* **2011**, *24*, 32.
- [4] B. Yan, S.-C. Zhang, *Rep. Prog. Phys.* **2012**, *75*, 096501.
- [5] Y. Wang, Y. Ding, *Phys. Chem. Chem. Phys.* **2015**, *17*, 27769.
- [6] S. Zhang, Z. Yan, Y. Li, Z. Chen, H. Zeng, *Angew. Chem. Int. Ed.* **2015**, *54*, 3112.
- [7] G. Wang, R. Pandey, S. P. Karna, *ACS Appl. Mater. Interfaces* **2015**, *7*, 11490.
- [8] O. U. Akturk, V. O. Ozcelik, S. Ciraci, *Phys. Rev. B* **2015**, *91*, 23.
- [9] D. Hsieh, Y. Xia, L. Wray, D. Qian, A. Pal, J. H. Dil, J. Osterwalder, F. Meier, G. Bihlmayer, C. L. Kane, Y. S. Hor, R. J. Cava, M. Z. Hasan, *Science* **2009**, *323*, 919.
- [10] G. Bian, X. Wang, P. J. Kowalczyk, T. Maerkl, S. A. Brown, T.-C. Chiang, *J. Phys. Chem. Solids* **2019**, *128* 109.
- [11] A. Narayan, I. Rungger, S. Sanvito, *Phys. Rev. B* **2012**, *86*, 20.
- [12] D. Campi, M. Bernasconi, G. Benedek, *Phys. Rev. B* **2012**, *86*, 7.
- [13] G. Bian, T. Miller, T.-C. Chiang, *Phys. Rev. Lett.* **2011**, *107* 036802.
- [14] G. Bian, X. Wang, Y. Liu, T. Miller, T.-C. Chiang, *Phys. Rev. Lett.* **2012**, *108*, 176401.
- [15] P. Zhang, Z. Liu, W. Duan, F. Liu, J. Wu, *Phys. Rev. B* **2012**, *85*, 201410(R).
- [16] G. Yao, Z. Luo, F. Pan, W. Xu, Y. P. Feng, X. S. Wang, *Sci. Rep.* **2013**, *3*, 2010.
- [17] N. Nouri, M. Bieniek, M. Brzeziaska, M. Modarresi, S. Z. Borujeni, G. Rashedi, A. Wojs, P. Potasz, *Phys. Lett. A* **2018**, *382*, 2952.
- [18] K. An, C. Hwang, Y. Kim, E. Cho, C. Park, A. Kakizaki, *Surf. Sci.* **2001**, *492*, L705.
- [19] W. Slijberman, P. Zagwijn, J. van der Veen, D. Gravesteijn, G. van de Walle, *Surf. Sci.* **1992**, *262*, 25.
- [20] M. Stróak, M. Kopciuszyski, A. Stepniak-Dybala, M. Krawiec, M. Jaochowski, *Condens. Matter* **2016**, *1*, 11.
- [21] T. D. Golding, J. A. Dura, W. C. Wang, A. Vigliante, S. C. Moss, H. C. Chen, J. H. Miller, C. A. Hoffman, J. R. Meyer, *Appl. Phys. Lett.* **1993**, *63*, 1098.
- [22] J. Guyaux, R. Sporken, R. Caudano, V. Wagner, J. Geurts, N. Esser, W. Richter, *Surf. Sci.* **1995**, *338*, 204.
- [23] H. Toyota, A. Okabe, T. Endoh, Y. Jinbo, N. Uchitomi, *J. Cryst. Growth* **2013**, *378*, 129.
- [24] Y. Zhou, E. Wang, *J. Appl. Phys.* **1998**, *84*, 4309.
- [25] H. Pan, X.-S. Wang, *Nanoscale Res. Lett.* **2015**, *10*, 334.
- [26] B. Bennett, B. Shanabrook, R. Wagner, J. Davis, J. Waterman, *Appl. Phys. Lett.* **1993**, *63*, 949.
- [27] J. E. Bickel, C. Pearson, J. M. Millunchick, *Surf. Sci.* **2009**, *603*, 14.
- [28] E. M. Anderson, J. M. Millunchick, *J. Cryst. Growth* **2018**, *500* 68.
- [29] X. Yi, H. Wang, S. Chen, J. Lai, M. He, S. Wang, G. K. Wong, *Infrared Phys. Technol.* **2005**, *46*, 263.
- [30] G. Bell, T. Jones, C. McConville, *Appl. Phys. Lett.* **1997**, *71*, 3688.
- [31] G. Bell, C. McConville, T. Jones, *Appl. Surf. Sci.* **1996**, *104*, 17.
- [32] K. Szamota-Leandersson, M. Leandersson, M. Gathelid, U. O. Karlsson, *Surf. Sci.* **2011**, *605*, 12.
- [33] F.-C. Chuang, C.-H. Hsu, C.-Y. Chen, Z.-Q. Huang, V. Ozolins, H. Lin, A. Bansil, *Appl. Phys. Lett.* **2013**, *102*, 022424.
- [34] S. Ichikawa, N. Sanada, N. Utsumi, Y. Fukuda, *J. Appl. Phys.* **1998**, *84*, 3658.
- [35] E. Hilner, E. Lundgren, A. Mikkelsen, *Surf. Sci.* **2010**, *604*, 354.
- [36] S. Mankefors, P. Nilsson, J. Kanski, *Surf. Sci.* **1999**, *443*, L1049.
- [37] S. Tanuma, C. J. Powell, D. R. Penn, *Surf. Interface Anal.* **35**, 268.
- [38] L. Winterfeld, C. Koppka, D. Abou-Ras, P. Kleinschmidt, O. Supplie, T. Hannappel, E. Runge, *Phys. Rev. Mater.* **2018**, *2*, 12.
- [39] C. Koppka, A. Paszuk, M. Steidl, O. Supplie, P. Kleinschmidt, T. Hannappel, *Cryst. Growth Des.* **2016**, *16*, 6208.
- [40] M. W. Wang, *J. Vac. Sci. Technol. B: Microelectron. Nanometer Struct.* **1993**, *11*, 1418.
- [41] S. Hatfield, G. Bell, *J. Cryst. Growth* **2006**, *296*, 165.
- [42] D. Rioux, H. Hoehst, *J. Appl. Phys.* **1993**, *74*, 3497.
- [43] W. C. Wang, J. A. Dura, J. T. Zborowski, A. Vigliante, H. C. Chen, T. D. Golding, J. R. Meyer, *J. Vac. Sci. Technol. A: Vac. Surf. Films* **1993**, *11*, 1001.
- [44] B. Stegemann, C. Ritter, B. Kaiser, K. Rademann, *Phys. Rev. B* **2004**, *69*, 15.
- [45] C. S. Barrett, P. Cucka, K. Haefner, *Acta Crystallogr.* **1963**, *16*, 451.
- [46] P. Mousley, C. Burrows, M. Ashwin, A. Sanchez, V. Lazarov, G. Bell, *J. Cryst. Growth* **2018**, *498* 391.
- [47] C. Nicklin, T. Arnold, J. Rawle, A. Warne, *J. Synchrotron Radiat.* **2016**, *23*, 1245.
- [48] C. M. Schlepütz, R. Herger, P. R. Willmott, B. D. Patterson, O. Bunk, C. Brönnimann, B. Henrich, G. Hülsen, E. F. Eikenberry, *Acta Crystallogr. A: Found. Crystallogr.* **2005**, *61*, 418.
- [49] E. Vlieg, *J. Appl. Crystallogr.* **2000**, *33*, 401.
- [50] T. A. Petach, A. Mehta, M. F. Toney, D. Goldhaber-Gordon, *Phys. Rev. B* **2017**, *95*, 18.
- [51] S. Bengió, J. Wells, T. Kim, G. Zampieri, L. Petaccia, S. Lizzit, P. Hofmann, *Surf. Sci.* **2007**, *601*, 2908.
- [52] A. Jain, S. P. Ong, G. Hautier, W. Chen, W. D. Richards, S. Dacek, S. Cholia, D. Gunter, D. Skinner, G. Ceder, K. A. Persson, *APL Mater.* **2013**, *1* 011002.